Topological insulator n-p-n junction in a magnetic field: Supplementary Information

A. Sample preparation and device fabrication

BSTS single crystals were prepared by modified Bridgman technique in a home-built furnace. Stoichiometric amounts of high purity starting materials(99.999%) were sealed in evacuated quartz ampoules($\sim 10^{-5}$ mbar) and heated to 850°C followed by slow cooling to room temperature. Single crystals as large as ∼10mm can be obtained as shown in Fig. S1(a). Single crystals were characterized by X-ray diffraction(Fig. S1(b)), bulk electrical transport measurements, Energy dispersive X-ray spectroscopy, Electron probe microanalysis and Angle Resolved photoemission spectroscopy(ARPES) measurements as shown in our previous works. Specifically, ARPES measurements[8] confirm that the chemical potential in our samples lies within the bulk band-gap, a primary requirement to obtain highly gate-tunable topological insulator devices.

For device fabrication, we first exfoliate thin flakes of BSTS and hexagonal Boron Nitride(h-BN) from BSTS single crystals and commercial h-BN powder(Momentive) respectively onto two separate pieces of heavily doped p-type Silicon substrates coated with 285/500 nm of SiO_2. A transparent polymer stack consisting of polypropylene-carbonate(PPC) spin-coated on polydimethylsiloxane(PDMS) films stuck to a glass substrate is fixed to a micromanipulator stage. Using a custom-built setup housed in an Argon glove box(<0.1 ppm O_2), the polymer stack is used to pick up a suitable h-BN flake from the SiO_2 substrate. This flake is then aligned with micrometer precision to a suitable flake of BSTS. The glass substrate is lowered until the h-BN and BSTS flakes are in contact. After desirable alignment and contact between the two flakes is obtained, the polymer stack is heated at $\sim$ 80°C to melt the PPC layer which causes the h-BN flake to drop down. The residual PPC is later removed by cleaning the sample in chloroform and acetone. Subsequently, standard e-beam lithography is used to define electrical contacts followed by e-beam evaporation of Cr/Au(10nm/70nm). Fig. S1(c) shows optical micrograph images of representative devices.

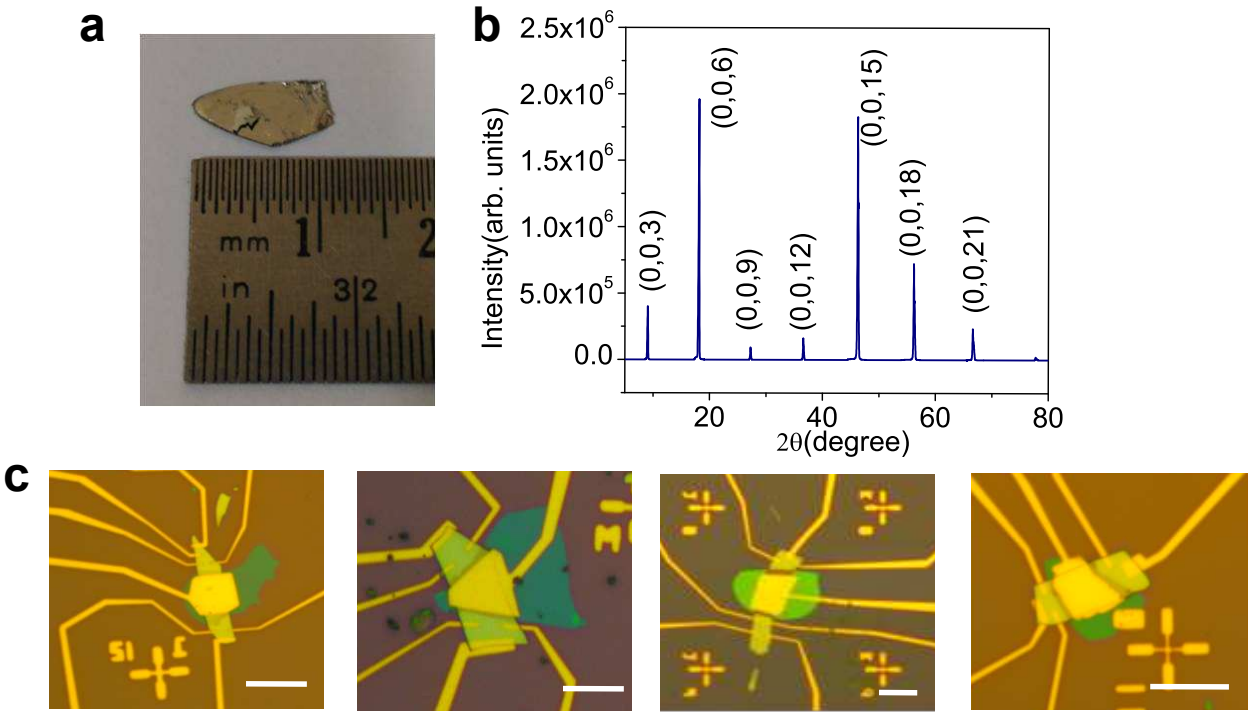

FIG. S1. (a) Single crystal of $BiSbTe_{1.75}Se_{2.25}$(b) X-ray diffractogram showing only (0,0,L) peaks confirming single crystalline nature (c) Optical micrographs of h-BN/BSTS n-p-n type devices. Scale bar=10 μm

B. Estimation of number of surface state channels using magnetoresistance measurements

We employ magnetoresistance measurements to estimate the number of surface states in our samples. Even in compensation doped topological insulator samples that appear to be bulk-insulating, residual bulk conduction may not be fully suppressed at low temperatures. Bulk carriers may therefore provide parasitic paths between the top and bottom topological surface states, resulting in an effective surface state coupling. The presence of such coupling may dramatically alter the properties expected from p-n junctions of ideal topological surface states, apart from inducing coupling between quantum Hall edge states via residual bulk modes. To verify this is not the case, we use the weak anti-localization(WAL) response of topological surface states to a perpendicular magnetic field to estimate the number of surface states carriers. Magnetoresistance data is fitted to HLN formula that described the weak anti-localization effect in a perpendicular magnetic

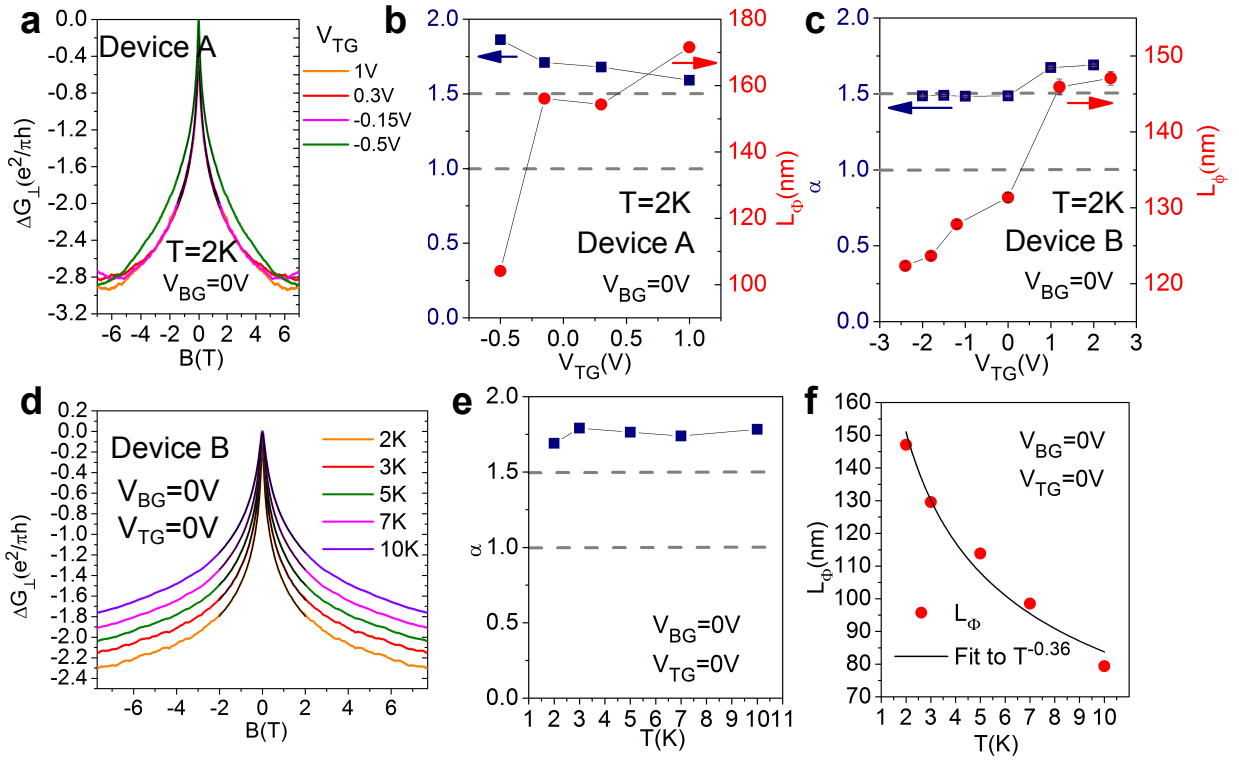

FIG. S2. (a) Magnetoconductance for device A at different values of the top gate voltage V_{TG} (b) and (c) α and L_ϕ as a function of V_{TG} extracted by HLN fits to (a) for devices A and B respectively.(d) Magnetoconductance at different temperatures measured in device B. (e) α and (f) L_ϕ extracted from HLN fits to (d)

field[3,6,9]:$\Delta G_{xx}(B) = -\alpha\frac{e^2}{2\pi^2\hbar}\left[\psi\left(\frac{1}{2}+\frac{\hbar}{4eL_\phi^2 B}\right) - \ln\left(\frac{\hbar}{4eL_\phi^2 B}\right)\right]$ in the limit of strong spin-orbit scattering. Here ΔG_{xx} is the change in sample conductivity, B is the applied magnetic field, L_ϕ is the phase coherence length, and $\psi(x)$ denotes the digamma function. The leading constant α determines the number of *uncoupled* spin-orbit coupled channels, with a value of 0.5 for each such channel. As shown in Fig. S2(a), a sharp cusp in conductance at zero magnetic field indicates the presence of weak-anti localization effects. We measure magnetoconductance for devices A and B at different values of the top gate voltage. As shown in Fig. S2(b) and (c), the phase coherence length L_ϕ drops significantly in the hole-doped regime compared to the electron doped regime, presumably due to lower electron mobility on the hole-side. On the other hand, $\alpha = 1.5 \sim 2$ remains fairly constant in the entire range of gate voltage. Most remarkably, this value of α represents the presence of 3-4 independent spin-orbit coupled channels that carry electrical current in our devices. These

channels represent the top and bottom topological surface states, and the top and bottom Rashba surface surface states. In samples that are thinner than $\sim$ 30-40nm, the two Rashba surface states get coupled due to inter-band scattering and contribute to the WAL effect as a single channel(giving α=1.5). This effect has been explored in detail in our previous work[1]. For the present work, it suffices to show that the top and bottom topological surface states are decoupled in our system, and they indeed contribute to electrical transport as two separate channels. However in the quantum Hall regime, the presence of Rashba states may interfere with the quantum Hall effect of the top/bottom topological surface states. This possibility has been discussed in the main text(Sec: Discussion). We also explore the WAL signature as a function of temperature, as shown in Fig. S2(d) for device B. While $\alpha \sim 1.5$ remains roughly constant as a function of temperature till $T \sim 10K$, L_ϕ shows a temperature dependent decay as a power law given by $T^{-0.36}$.

C. Estimation of carrier concentration and mobility

We perform Hall effect measurements to estimate the carrier concentration and mobility in our devices. Fig. S3(a) shows the variation of the Hall resistance R_{xy} as a function of magnetic field in the range from -7T to +7T at different values of the top gate voltage. At positive values of V_{TG} , the slope of R_{xy} vs. B is negative indicating n-type carriers. As the top gate voltage is changed from positive to negative, the carrier type changes sign as indicated by a change in slope of the Hall effect curves. The extracted carrier concentration and mobility is shown in Fig. S3(b). In Fig. S3(c), we plot Hall resistance at different temperatures at zero applied gate voltages. As shown in Fig. S3(d), with increasing temperature, the carrier concentration increases while the carrier mobility plummets. This behavior is a consequence of the compensation doping of our samples, and can be explained as a consequence of activated hopping transport across a network of p-n junctions[1]. We note that our analysis of Hall effect measurement is close to charge neutrality in our samples. Such an analysis is intrinsically prone to error because electrical current is carried by both electrons and holes in this regime and Hall effects from the two carrier types cancel each other out, resulting in 'zero' slope. This leads to an overestimation of the carrier concentration($n = \frac{B}{R_{xy}e}$) and an underestimation of the Hall mobility.

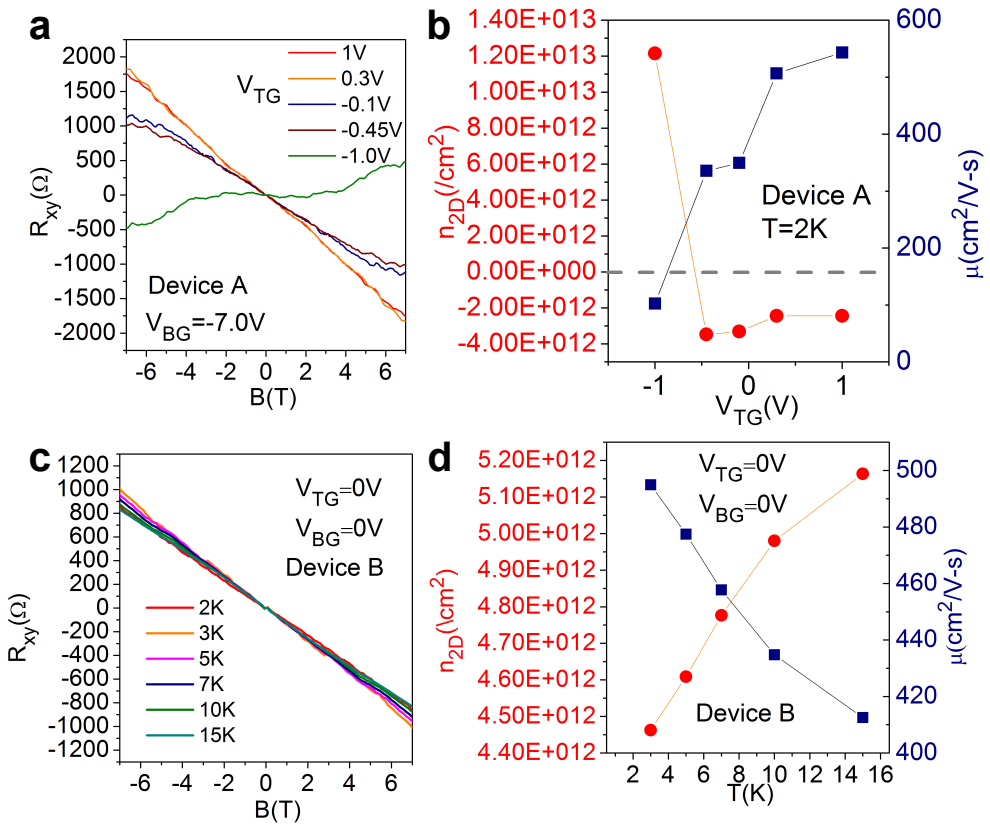

FIG. S3. (a) Hall effect measurement for device A at different values of top gate voltage V_{TG} . (b) Extracted carrier concentration and carrier mobility (c) Hall effect measurement in Device B at different sample temperatures (d) Extracted carrier concentration and mobility at different sample temperatures

D. Conductance fluctuations and tracking the charge neutrality peaks

The position of the two charge neutrality peaks varies as a function of both top and bottom gate voltages(Fig. S4(a)).The cross-coupling between the top(bottom) surface state chemical potential and the bottom(top) gate can be evaluated by measuring the tilt of the trajectory of the charge neutrality point away from vertical(horizontal) axis in the V_{TG} - V_{BG} space, and is mediated by an inter-surface state coupling capacitance. While the bare R_{xx} vs (V_{TG} -V_{BG}) data does feature this information(S4(b)), tracking the exact location of the charge neutrality point becomes more effective by measuring conductance fluctuations instead.

In Fig. S4(a) and (b), we plot the conductance fluctuations obtained from devices A and

B at T=2K. This is obtained by subtracting a smooth background from the raw R_{xx} vs (V_{TG} -V_{BG}) data. Both devices show reproducible resistance fluctuations that follow well-defined trajectories in the (V_{TG} -V_{BG}) space. While these trajectories are clearly tilted away from the horizontal/vertical axes, it is interesting to note that the trajectories are not perfect straight lines. In fact, they are straight only near the charge neutrality points (CNP). Away from CNP, these lines appear to deviate. This arises as a result of quantum capacitance of the top and bottom topological surface states (TSS). We must bear in mind that although the top/bottom TSS are metallic, they are characterized by zero density of states at the Dirac point(unlike a true metal). This implies that charging of the two surface states is governed not by the geometric capacitance of the device, but instead by the quantum capacitance of the two TSS near CNP. On the other hand, as one moves away from CNP, the quantum capacitance increases and eventually exceeds the geometric capacitance. At this point, the charging of the device is governed by the geometric capacitances of the sample. This effect is reproduced in our model calculations in Section E where clear deviations of the CNP trajectories away from straight line trajectories are observed.

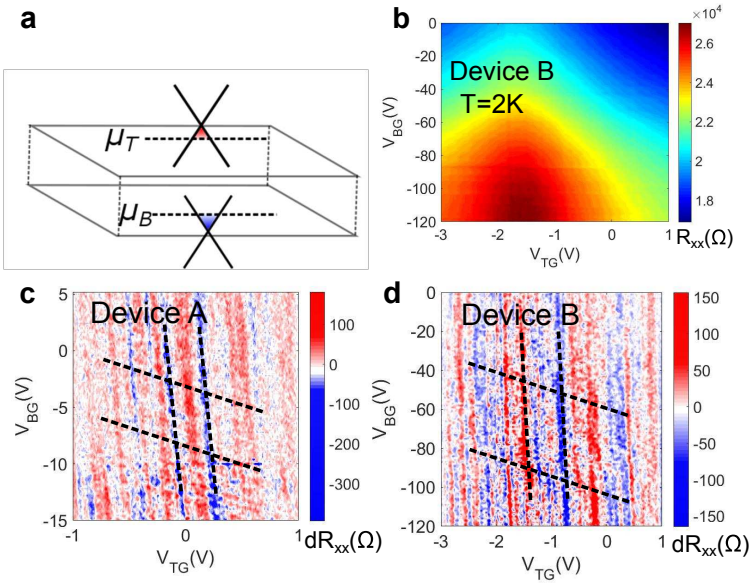

FIG. S4. (a) Schematic of a TI slap with two different top and bottom surface state chemical potentials (b) 2D map of R_{xx} vs V_{TG} -V_{BG} for device B at T=2K. (c) and (d) Conductance fluctuations measured in devices A and B as a function of V_{TG} -V_{BG} . Dashed lines are guides to the eye showing trajectories of conductance fluctuation peaks(dips)

E. Electrostatic model

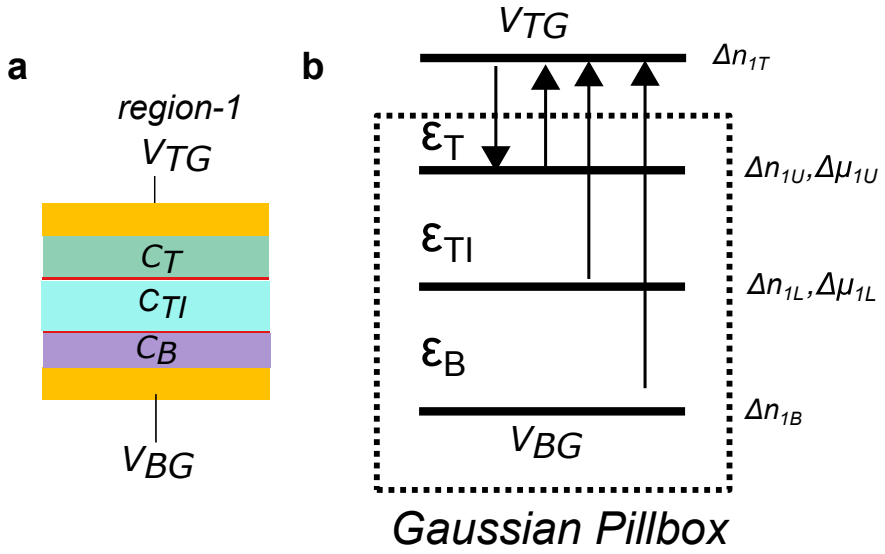

FIG. S5. (a) Capacitance model of the top-gated region(region-1) (b) Gaussian pillbox method for evaluating the electric field in the three different dielectrics

We use a charging model analysis[2,7] to derive the electrostatics of the top-gated(region-1) and back-gated(region-2) regions separately.

Region-1

For the top-gated region shown schematically in Fig. S5(a), we derive the following equations from charge conservation and voltage balance: From total charge conservation, we obtain:

$$\Delta n_{1T} + \Delta n_{1U} + \Delta n_{1L} + \Delta n_{1B} = 0 \tag{1}$$

Next, we determine the electric field within each of the three capacitances, using a Gauss' law. For example, to evaluate the electric field within the top-gate dielectric, we use a Gaussian pillbox as shown in Fig. S5(b). The electric fields from each of the four metallic surfaces is given as $E_j = \Delta n_j/2\epsilon_T$ where n_j is the charge density on surface j, and ϵ_T is the dielectric constant of the top-gate dielectric. The electric field at any point within the dielectric of the top gate is given as $E_T = e(\Delta n_{1T} - \Delta n_{1U} - \Delta n_{1L} - \Delta n_{1B})/2\epsilon_T =$

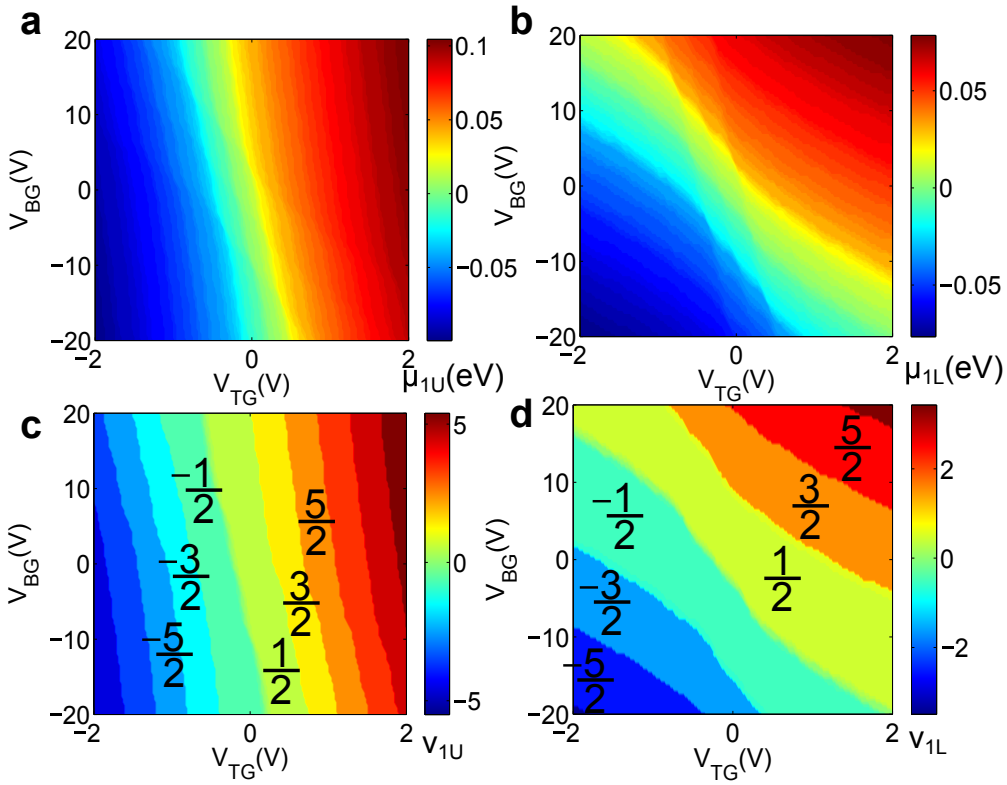

FIG. S6. (a) Top surface chemical potential and (b) bottom surface chemical potential as a function of V_{TG} and V_{BG} . (c) Top surface filling factor and (b) bottom surface filling factor as a function of V_{TG} and V_{BG}

$e\Delta n_{1T}/\epsilon_T$(using Eq. 1). From voltage balance across this dielectric layer, we obtain:

$$V_{TG} - E_T t_T = e\Delta\mu_{1U} \tag{2}$$

$$\implies V_{TG} - \Delta n_{1T} t_T/\epsilon_T = e\Delta\mu_{1U} \tag{3}$$

$$\implies V_{TG} - \Delta n_{1T}/C_T = e\Delta\mu_{1U} \tag{4}$$

where t_T is the thickness of the top dielectric, and C_T is the top gate capacitance.

Similarly we derive two other voltage balance equations:

$$V_{BG} - \Delta n_{1B}/C_T = e\Delta\mu_{1L} \tag{5}$$

$$e(\Delta\mu_{1U} - \Delta\mu_{1L}) + (\Delta n_{1T} + \Delta n_{1U} - \Delta n_{1L} - \Delta n_{1B})/2C_{TI} = 0 \tag{6}$$

It is convenient to express the top and bottom gate voltages as a function of other

parameters, this gives us the following equations:

$$V_{TG} = \Delta\mu_{1U} - \frac{1}{C_T}\left[C_{TI}(\Delta\mu_{1L} - \Delta\mu_{1U}) - \Delta n_{1U}\right] \tag{7}$$

$$V_{BG} = \Delta\mu_{1L} - \frac{1}{C_B}\left[C_{TI}(\Delta\mu_{1U} - \Delta\mu_{1L}) - \Delta n_{1L}\right] \tag{8}$$

From the geometric values obtained from thickness measurement of samples, we obtain the values of all capacitances. We take $t_T = 15nm$, $t_B = 500nm$ and $t_{TI} = 20nm$. The values of dielectric constants are taken from previously reported values to be $\epsilon_T = 3$, $\epsilon_B = 3.9$ and $\epsilon_{TI} = 33$. By solving these equations numerically, we obtain values of chemical potentials ($\Delta\mu_{1U,L}$) and charge carrier densities($\Delta n_{1U,L}$). The simulated chemical potentials on the upper and lower surfaces of the TI flake as a function of V_{TG} and V_{BG} are shown in Figs. S6(a) and (b) respectively. In the presence of quantizing magnetic fields, Landau level formation takes place. Using the chemical potential, the Landau level index(n) can be obtained from the following relation for Dirac dispersions:

$$\mu = sign(m)\hbar\omega\sqrt{|m|} \tag{9}$$

where $m = 0, \pm1, \pm2, ...$ take integer values, $\omega = v_F\sqrt{2\pi B/\phi_0}$. Here v_F is the Fermi velocity of the Dirac dispersion measured previously in our ARPES experiments, $\phi_0 = h/2e$ is the flux quantum and B is the applied external magnetic field. Notice that the Dirac dispersion allows a zero energy LL state(Eq. 9) that does not move with changing magnetic field. This imparts a dual character to the zero-Landau level, in that, it gets shared equally by holes and electrons. This is the origin of the 1/2 filling factor of the zero LL, while all other LLs contribute a filling factor of 1: $\nu = sign(m)(|m| + 1/2)$ The charge density can then be obtained by multiplying the filling factor ν with the Landau level degeneracy factor(B/ϕ_0) giving $n = B\nu/\phi_0$

Using Eq. 9, we can now find the corresponding filling factors on each surface of region-1 as a function of V_{TG} and V_{BG} . These are plotted as 2D color maps in Figs. S6(c) and (d).

Region-2

In a fashion similar to region-1, we derive the electrostatic equations of region-2. The only difference here being that there is no boundary condition on the top surface, and the top-surface state chemical potential needs to be evaluated self-consistently. The governing

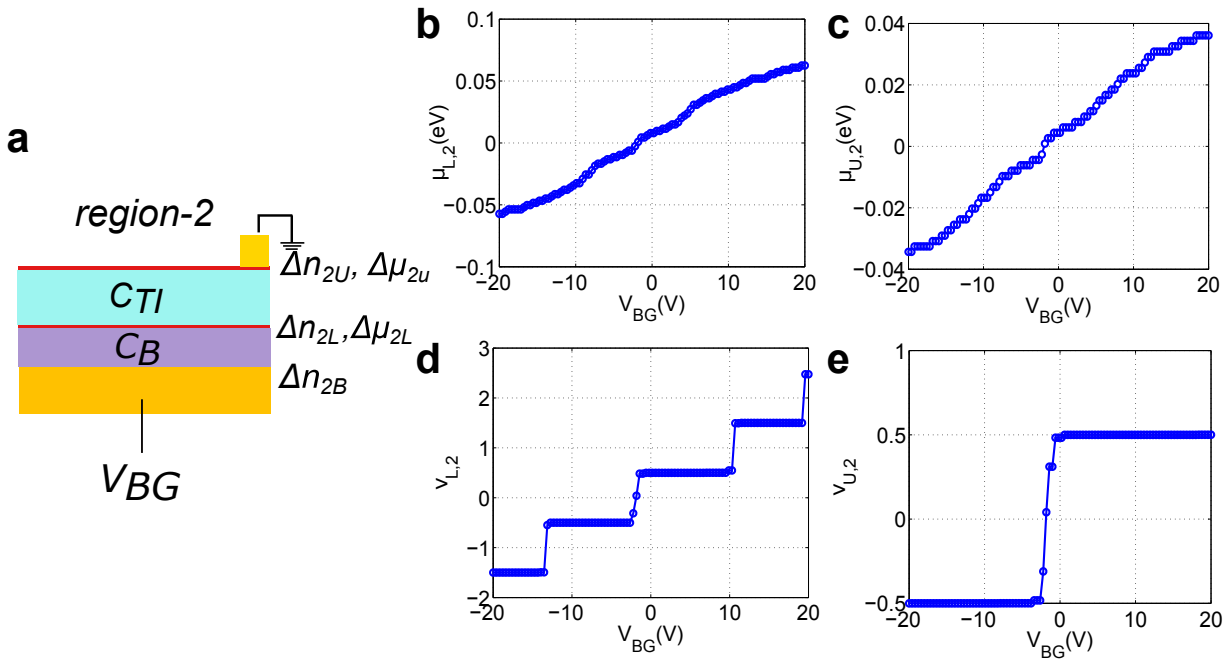

FIG. S7. (a) Capacitance model of the back-gated region(region-2). (b) Bottom surface state chemical potential, (c) top surface state chemical potential, (d) bottom surface state filling factor and (e) top surface state filling factor as a function of V_{BG}

equations are as follows:

$$\Delta n_{2U} + \Delta n_{2L} + \Delta n_{2B} = 0 \tag{10}$$

$$V_{BG} + \Delta n_{2B}/C_B = \Delta\mu_{2L} \tag{11}$$

$$\Delta n_{2U} = 2C_{TI}(\Delta\mu_{2L} - \Delta\mu_{2U}) \tag{12}$$

Using this we simulate the action of the back gate voltage V_{BG} on the chemical potentials of the bottom and top surface states. These are plotted in Fig. S7(b) and (c) respectively. It is clear that the bottom gate exerts a much stronger control on the bottom surface state chemical potential μ_{2L} than on the top surface chemical potential μ_{2U}. The corresponding filling factor diagrams are plotted in Fig. S7(d) and (e).

F. Landauer-Buttiker formalism for edge state propagation

To determine the four terminal resistance in a configuration with strong electron density gradients, we use the Landauer-Buttiker formalism[4,5,10]. First, we derive a general relation

that is applicable to quantum Hall effect in any system with carrier density gradients.This formula is then applied to the three cases discussed in the main text.

General formula

The Landauer resistance formula for multi-channel, multi-probe transport is given as:

$$I_i = \frac{e}{h}\left[(M_i - R_{i,i})\mu_i - \sum_{j\neq i} T_{i,j}\mu_j\right] \tag{13}$$

Where I_i is the current from the reservoir at contact i, M_i is the number of channels in contact i, $R_{i,i}$ is the total probability of reflection in contact i from all other contacts, and $T_{i,j}$ is the transmission probability from contact i to contact j. Conservation of current yields the relation that $R_{i,i} = M_i - \sum_{j\neq i} T_{i,j}$.

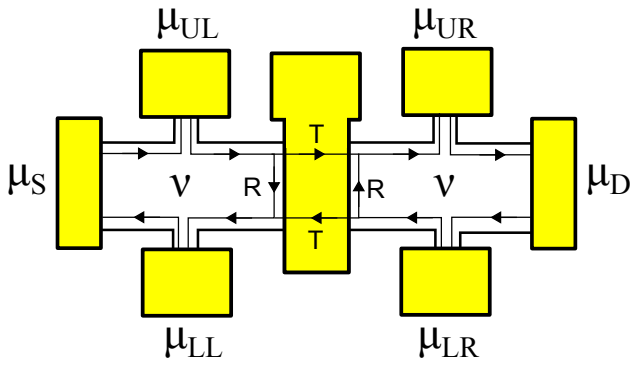

FIG. S8. Schematic of Hall bar with density gradient at the center induced by a local top-gate electrode. The filling factor in the un-gated region is ν. T and R are the transmission and reflection probabilities of edge states across the top-gated region.

We consider a Hall bar sample with a density gradient induced by a top gate as shown in Fig. S8. The filling factor in the non-gated region is ν. At this point, we model the top-gated region as a scattering center, that can either transmit edge states with a probability T or reflect them with probability R. S and D are the current source and drain respectively, while the other four nodes are voltage probes. Applying Eq. 13 to nodes UL and S we obtain the following two equations:

$$0 = \frac{e}{h}\nu(\mu_{UL} - \mu_S) \tag{14}$$

$$I = \frac{e}{h}\nu(\mu_S - \mu_{LL}) \tag{15}$$

Combining these equations and repeating for nodes LR and D, we obtain the results for standard quantum Hall effect:

$$I = \frac{e}{h}\nu(\mu_{UL} - \mu_{LL}) = \frac{e}{h}\nu(\mu_{UR} - \mu_{LR}) \tag{16}$$

The effect of the gate-induced density gradient become apparent when we evaluate Eq. 13 at nodes LL and UR. For example, at node LL, edge modes can be transmitted from node LR by transmission over the gated region with probability T, and from node UL by reflection at the gated region with probability R. We can therefore write:

$$0 = \frac{e}{h}\nu(\mu_{LL} - T\mu_{LR} - R\mu_{UL}) \tag{17}$$

Similarly, for node UR, we can write:

$$0 = \frac{e}{h}\nu(\mu_{UR} - T\mu_{UL} - R\mu_{LR}) \tag{18}$$

The four terminal resistance is given by $R_U = (\mu_{UL} - \mu_{UR})/eI$. By combining the above equations, and using the fact that T+R=1, we obtain the following relation:

$$R_U = \frac{h}{e^2}\left(\frac{1}{T\nu} - \frac{1}{\nu}\right) \tag{19}$$

It is important to note that in our analysis, we did not make any assumptions about the direction in which edge modes circulate in the gated region. That is, we could very well have modes in the gated region, that travel in a direction opposite to that shown in Fig. S8. The only assumption we use is R+T=1, which is justified by current conservation since no additional current can be sourced or sunk in the gated region. This allows us to use this relation in any general setting where quantum Hall modes propagate across carrier density gradients. Only a case-by-case evaluation of the transmission probability T is required, as follows:

Case-1: Unipolar regime with $\nu_1 < \nu_2$

In this regime, ν_2 modes propagate in the un-gated region and a smaller number of ν_1 modes propagate in the gated region as shown in Fig. S9(a).

Only the occupied modes carrying current from the left-lead to the right-lead are shown. From the band-structure of Fig S9(b), it is clear that the mode(shown in blue) that is

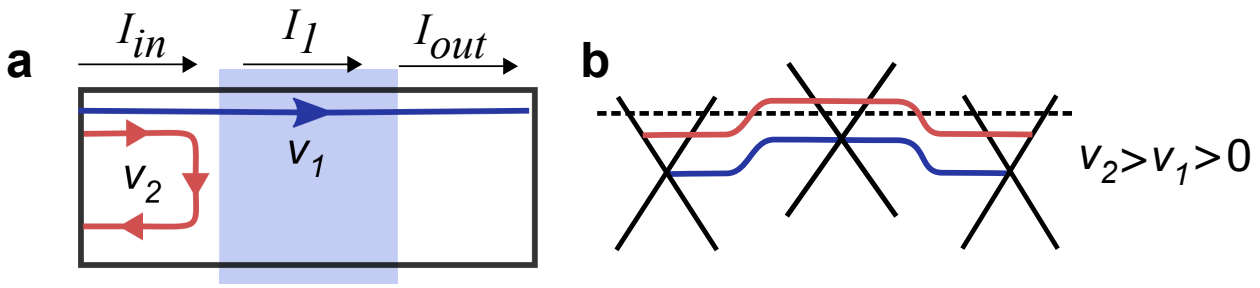

FIG. S9. (a) Edge state propagation in the unipolar regime with $\nu_1 < \nu_2$. (b) Band-structure diagram as a function of position.

common to both the regions, propagates fully. Also, note that at the un-gated/gated region interface, this mode does not cross the Fermi level, that is it does not propagate along the interface. On the other hand, the excess mode in the un-gated region(shown in red) does cross the Fermi level at the un-gated/gated region interface, and propagates not only along the sample edge but also along the interface as shown in Fig. S9(a).

To evaluate the four-probe resistance, we need only to evaluate the transmission probability across the gated region, $I = I_{out}/I_{in}$. Since there are no excess modes in the gated region, $I_{out} = I_1 = (\nu_1/\nu_2)I_{in}$. This gives us $T = (\nu_1/\nu_2)$. Applying Eq. 19, we get:

$$R_U = \frac{h}{e^2}\left(\frac{1}{\nu_1} - \frac{1}{\nu_2}\right) \tag{20}$$

Case-2: Unipolar regime with $\nu_1 > \nu_2$

In this regime, the number of edge modes in the gated region ν_2 is larger than the number of modes in the un-gated region ν_1 as shown in Fig. S10(a). The band-structure shown in Fig. S10(b) shows that all edge modes common to both the regions(shown in blue) propagate from the left-lead to right lead without intersecting the Fermi level at the un-gated/gated region interface. On the other hand, the excess modes in the gated region(shown in red) intersect the Fermi level and therefore also propagate parallel to the un-gated/gated interface as shown in Fig. S10(a).

To evaluate the transmission probability, we first note that in the gated region, under the assumption of full mode mixing, the current I_1 gets equally distributed among the ν_1 common modes(blue) and the $\nu_1 - \nu_2$ excess modes(red). We therefore obtain the following relations: $I_1 = I_{in} + I_4$, $I_{out} = I_2 - I_1$, $I_2 = (\nu_1 - \nu_2)/\nu_1$,$I_1 = rI_1$, $I_3 = I_2$, $I_4 = rI_3$. This

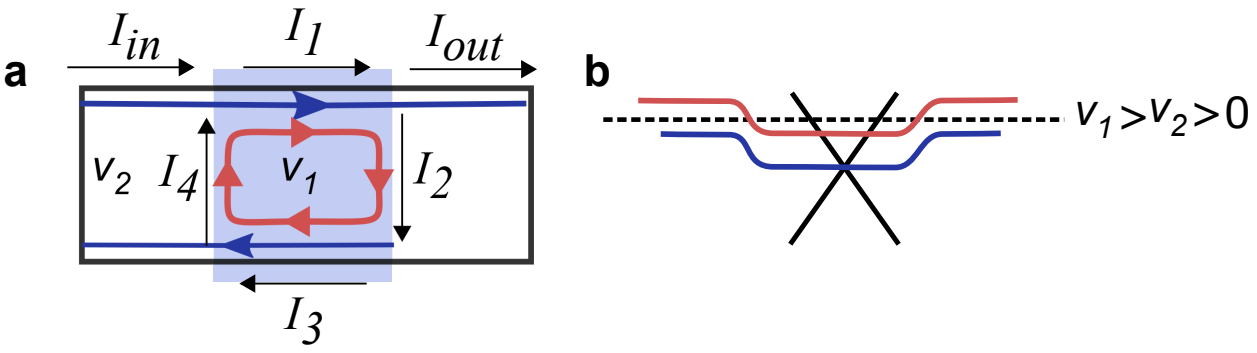

FIG. S10. (a) Edge state propagation in the unipolar regime with $\nu_1 > \nu_2$. (b) Band-structure diagram as a function of position.

gives, $I_{out} = (1-r)I_1$ and $I_{in} = I_1 - I_4 = (1-r^2)I_1$. Therefore the transmission probability $T = I_{out}/I_{in} = 1/(1+r) = \nu_1/(2\nu_1 - \nu_2)$. Substituting into Eq. 19, we obtain:

$$R_U = \frac{h}{e^2}\left(\frac{1}{\nu_2} - \frac{1}{\nu_1}\right) \tag{21}$$

Case-1: Bipolar regime with $\nu_1 < 0, \nu_2 > 0$

In the bipolar regime, the edge modes in the gated and un-gated regions propagate with opposite chiralities. Therefore, no common mode appears between the two regions. The only way current can flow from the left-lead to the right-lead is by mixing at the gated/ungated interface where modes from both region co-propagate as shown in Fig. S11(a). The band-structure diagram in Fig. S11(b) makes this adequately clear. All modes, originating either in the ungated region(blue) or the gated region(red) cross the Fermi level at the gated/ungated interface. This implies that all modes in the system are reflected at this interface. In the extreme case, that co-propagating modes do not fully mix at the interface, no current will flow from the left-lead to the right-lead. Here, we assume full mixing of modes, as would be the case in a moderately disordered sample, implying that current I_2 and I_4 are carried by $|\nu_1| + \nu_2$ number of modes.

To calculate the transmission probability, we obtain the following relations: $I_{out} = I_2 - I_1$, $I_{in} = I_4 - I_1$, $I_1 = rI_2 = |\nu_1|/(\nu_1 + |\nu_2|)I_2$, $I_2 = I_3$ and $I_3 = rI_4$. This gives $I_{out} = (1-r)I_2$ and $I_{in} = (1 - r^2/r)I_2$. Therefore we obtain: $T = I_{out}/I_{in} = |\nu_1|/(2|\nu_1| + \nu_2)$. Substituting into Eq. 19, we get:

$$R_U = \frac{h}{e^2}\left(\frac{1}{\nu_2} + \frac{1}{|\nu_1|}\right) \tag{22}$$

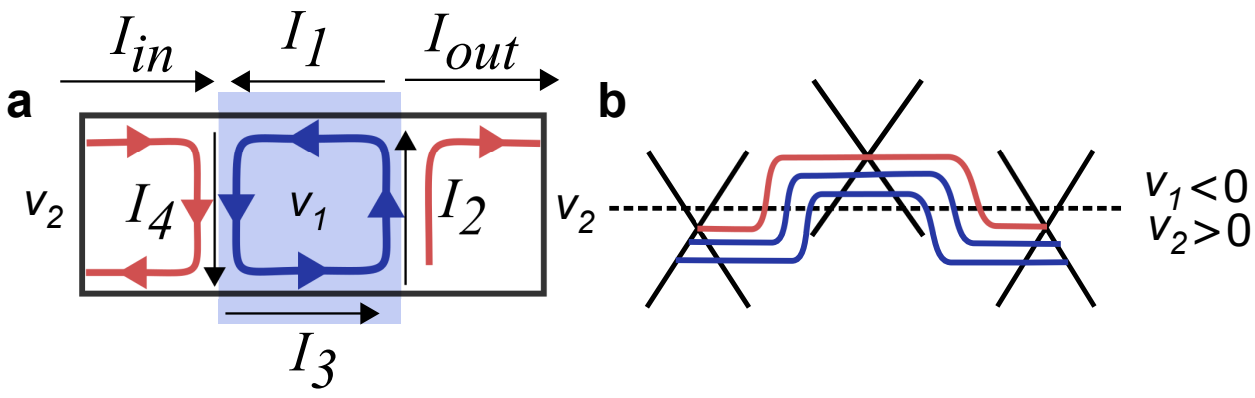

FIG. S11. (a) Edge state propagation in the bipolar regime with $\nu_1 < 0$ and $\nu_2 > 0$. (b) Band-structure diagram as a function of position.

[1] A. Banerjee, A. Sundaresh, K. Majhi, R. Ganesan, and P. S. A. Kumar, Appl. Phys. Lett., **109**, 232408 (2016).

[2] V. Fatemi, B. Hunt, H. Steinberg, S. L. Eltinge, F. Mahmood, N. P. Butch, K. Watanabe, T. Taniguchi, N. Gedik, R. C. Ashoori, and P. Jarillo-Herrero, Phys. Rev. Lett., **113**, 206801 (2014).

[3] I. Garate and L. Glazman, Physical Review B, **86**, 035422 (2012).

[4] R. Haug, Semiconductor science and technology, **8**, 131 (1993).

[5] R. J. Haug, A. H. MacDonald, P. Streda, and K. von Klitzing, Phys. Rev. Lett., **61**, 2797 (1988).

[6] S. Hikami, A. I. Larkin, and Y. Nagaoka, Progress of Theoretical Physics, **63**, 707 (1980).

[7] S. Kim, I. Jo, D. C. Dillen, D. A. Ferrer, B. Fallahazad, Z. Yao, S. K. Banerjee, and E. Tutuc, Phys. Rev. Lett., **108**, 116404 (2012).

[8] H. Lohani, P. Mishra, A. Banerjee, K. Majhi, M. Unnikrishnan, D. Topwal, P. S. A. Kumar, and B. R. Sekhar, Under Review (2016).

[9] H.-Z. Lu, J. Shi, and S.-Q. Shen, Phys. Rev. Lett., **107**, 076801 (2011).

[10] B. Özyilmaz, P. Jarillo-Herrero, D. Efetov, D. A. Abanin, L. S. Levitov, and P. Kim, Phys. Rev. Lett., **99**, 166804 (2007).